

<https://doi.org/10.1038/s41746-025-01850-5>

Phenotypic screening and genetic insights for predicting major vascular-related diseases using retinal imaging



Menglin Lu¹, Yiheng Mao¹, Hui Zhu¹, Yesheng Xu², Yu-Feng Yao^{2,3}, Fei Wu^{1,2}✉ & Zhengxing Huang^{1,2}✉

Retinal photography is a valuable non-invasive tool for assessing vascular health, but genetic evidence linking retinal microcirculation to major vascular-related diseases (e.g., myocardial infarction [MI], stroke, and chronic kidney disease [CKD]) remains scarce. This study investigates their relationships from both phenotypic and genetic perspectives. Phenotypically, we developed a retinal imaging-based screening model to evaluate 10-year risk of these conditions, incorporating quantitative analyses to pinpoint specific vascular abnormalities. Genetically, we analyzed retinal image-derived traits to explore their genetic and causal relationships with vascular-related diseases. Internal validation with 25,840 UK Biobank participants and external temporal validation with 4558 participants confirmed the model's superiority over traditional risk models. Mendelian randomization suggested causal relationships between retinal traits and stroke and MI, as well as the impact of CKD on retinal microcirculation. These findings reinforce the connection between retinal microcirculation and major vascular-related events, highlighting the potential of retinal imaging for early detection in clinical settings.

Retinal imaging has emerged as a potentially valuable tool for understanding human vasculature and assessing cardiovascular health^{1,2}. It allows non-invasive, in vivo assessment of the vascular system of the superficial inner retina, including the central and branch veins and arteries, as well as the venules and arterioles^{3,4}. Morphological changes in the retinal vessels often coincide with those in the microvasculature of other organs and may precede the progression of systemic vascular diseases³. As such, the retinal vasculature can provide supplementary insights into various systemic conditions, including an increased risk of obesity and cardiovascular diseases such as stroke^{5,6}, coronary heart disease^{7,8}, peripheral artery disease⁹, hypertension¹⁰, and atherosclerosis^{7,11}. By analyzing the retinal vasculature, early detection of these systemic diseases becomes possible, thereby enabling timely intervention and better management of vascular health¹².

The microcirculation of the heart, brain, and kidneys is a crucial component of systemic circulation¹³. Myocardial infarction (MI), stroke, and chronic kidney disease (CKD) are the primary indications of vascular dysfunction in these three essential organs. These major vascular-related events have high incidence and mortality rates, imposing a considerable burden on society^{3,14}. Previously established risk assessment models, such as the Framingham Risk Score (FRS)¹⁵, the Pooled Cohort Equation (PCE)^{16,17}, the QRISK3 model¹⁸, and the Systematic COronary Risk Evaluation (SCORE),

have been widely used in clinical practice to screen for these vascular-related diseases. However, these models rely on multiple indicators and often require blood tests and other measurements to gather the necessary data¹⁴. While cardiovascular imaging techniques like magnetic resonance imaging (MRI) are non-invasive, they can be relatively expensive¹⁴. In contrast, fundus images offer a non-invasive and cost-effective alternative to capture microvascular abnormalities, thereby aiding the development of early screening models for major vascular-related diseases, particularly in primary healthcare settings. Existing studies primarily analyze retinal image parameters, such as vessel caliber^{19–21}, fractal dimension^{22–24}, and vessel tortuosity^{25,26}, to identify biomarkers for various diseases and predict their onset. Recent advancements in artificial intelligence utilizing deep learning algorithms have indicated that retinal photographs can predict cardiovascular events with comparable accuracy to traditional cardiovascular disease risk assessment models^{14,27}. Furthermore, existing studies have demonstrated that deep learning models can effectively identify CKD and type 2 diabetes using fundus images alone or in combination with clinical metadata^{28–30}. These works often employ end-to-end deep learning models to learn the mapping from fundus images to different adverse events. Additionally, there are studies exploring the estimation of disease risk factors/biomarkers such as coronary artery calcium scores, left ventricular mass, and left ventricular end-

¹College of Computer Science and Technology, Zhejiang University, Hangzhou, China. ²Department of Ophthalmology, Affiliated Sir Run Run Shaw Hospital, School of Medicine, Zhejiang University, Hangzhou, China. ³Department of Ophthalmology, The Fourth Affiliated Hospital of Soochow University, Suzhou, China. ✉e-mail: wufei@zju.edu.cn; zhengxinghuang@zju.edu.cn

diastolic volume using retinal images, followed by utilizing these indicators to predict disease occurrence^{2,14,31}. This two-stage approach enhances the interpretability of the disease warning process.

Despite previous studies have attempted to utilize fundus images for early-stage screening of various vascular diseases, there remains a notable dearth of research that comprehensively combines major vascular-related events affecting the heart, brain, and kidneys, the microcirculation of which is an important part of the systemic microcirculation. As demonstrated in the previous study, assessing multiple diseases simultaneously using retinal imaging is a feasible approach³². Building upon this, our study aims to further explore the potential of combining MI, stroke, and CKD into a composite outcome, allowing us to leverage their interconnected pathophysiology to enhance predictive accuracy, as issues in one vascular domain often reflect systemic vascular health and can precipitate other diseases^{33,34}. This integrated model improves the efficiency of screening for vascular events, particularly in large-scale primary healthcare scenarios, thereby leading to earlier interventions and ultimately better patient outcomes^{35,36}. Furthermore, most existing studies focused on developing early screening models while neglecting quantitative analysis of retinal image microvascular features^{28,30}. These microvascular traits, which can vary among populations with different risks, offer valuable insights into vascular function and

structure. Additionally, it has been pointed out that studying the relationships across a spectrum of microvascular diseases affecting the retina, brain, kidney, and heart may uncover shared mechanisms that could inform novel treatment strategies^{13,37}. To the best of our knowledge, there is still a lack of systematic study that investigates the commonalities and differences in retinal morphological features associated with different vascular-related diseases. Moreover, prior studies on vascular disease screening using fundus images have often concentrated on constructing predictive models to explore phenotypic correlations, without specifically examining the genetic causality underlying these conditions. As a result, a definitive chain of evidence has not yet been established in this regard, inevitably hindering our understanding of the underlying genetic mechanisms involved in these diseases.

In this study, we aimed to analyze the association between retinal microcirculation and major vascular-related events from both phenotypic and genetic perspectives (Fig. 1). Phenotypically, we develop a fundamental model for the early screening of major vascular-related events in primary care, leveraging fundus photographs (FP) and minimal personal information (MPI). We hypothesized that retinal images provided crucial indications for vascular-related diseases, allowing us to screen major vascular-related events, such as stroke, MI, and CKD, using a deep learning model.

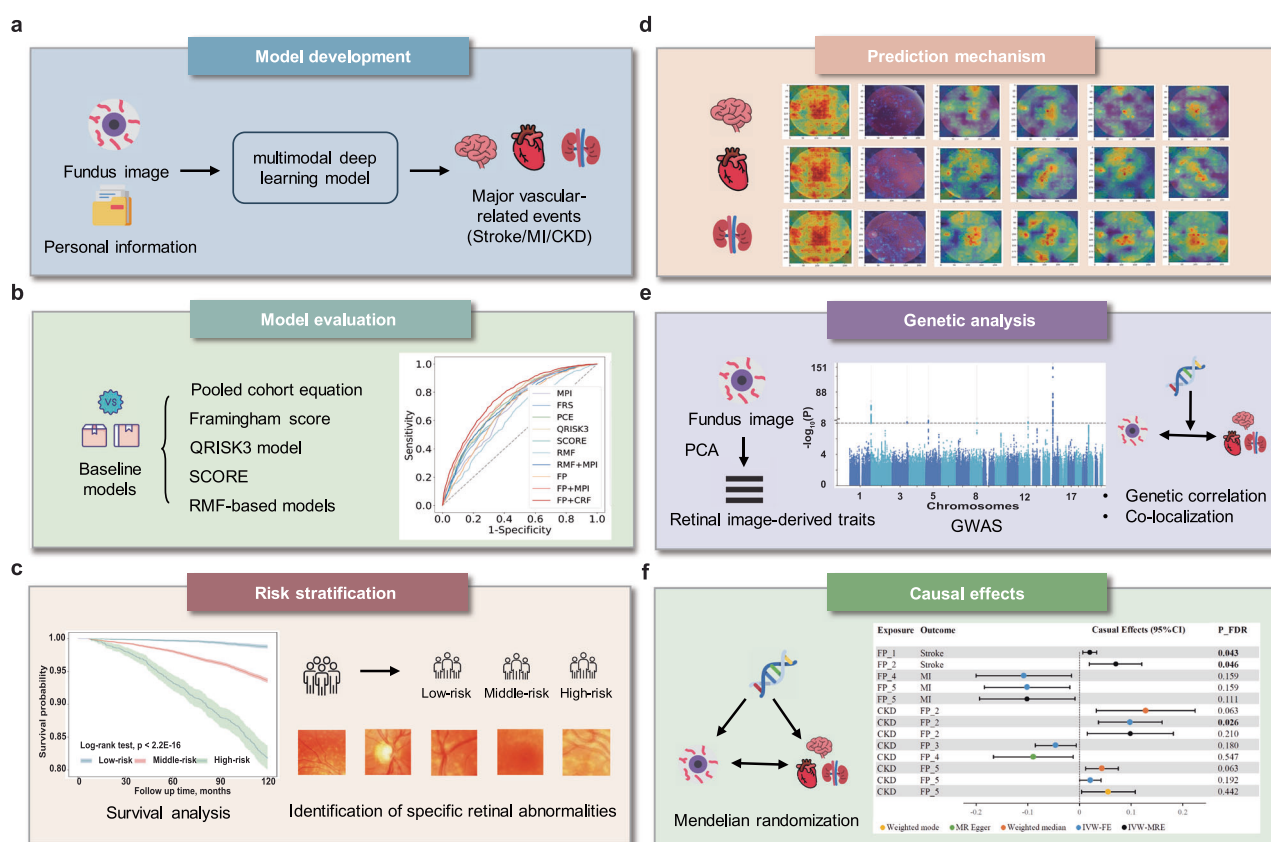


Fig. 1 | Study design. This figure depicts the research framework of this study to explore the association of retinal microcirculation with major vascular-related diseases from the phenotypic and genetic perspectives. **a** Deep learning for major vascular-related events prediction based on fundus images and personal information. **b** The proposed model was compared with traditional risk assessment models including PCE, FRS, QRISK3, and SCORE, and RMF-based models. **c** Kaplan–Meier curves depicting event occurrence rates across low, middle, and high-risk groups based on risk thresholds of 0.25 and 0.75 were plotted. Quantitative analysis of retinal microvascular parameters highlights differences in retinal indicators among risk groups was conducted. **d** Attention maps were plotted to explore the prediction mechanisms of our model for three vascular-related diseases based on retinal images. **e** Genetic analysis of retinal image-derived traits: Retinal features were extracted

using our model and reduced to 5 dimensions via PCA, preserving 90% of the information. GWAS was performed to pinpoint lead SNPs, and genetic correlation and colocalization analyses were conducted to validate the shared genetic basis between retinal image-derived traits and vascular-related diseases. **f** Causal effects between retinal image-derived traits and three vascular-related diseases were estimated using MR. AUC area under the receiver operating characteristic curve, CKD chronic kidney disease, CRF clinical risk factor, FP fundus photograph, FRS Framingham Risk Score, GWAS genome-wide association study, MI myocardial infarction, MPI minimal personal information, MR Mendelian randomization, PCA principal component analysis, PCE pooled cohort equation, RMF retinal microvascular features, SCORE systematic coronary risk evaluation.

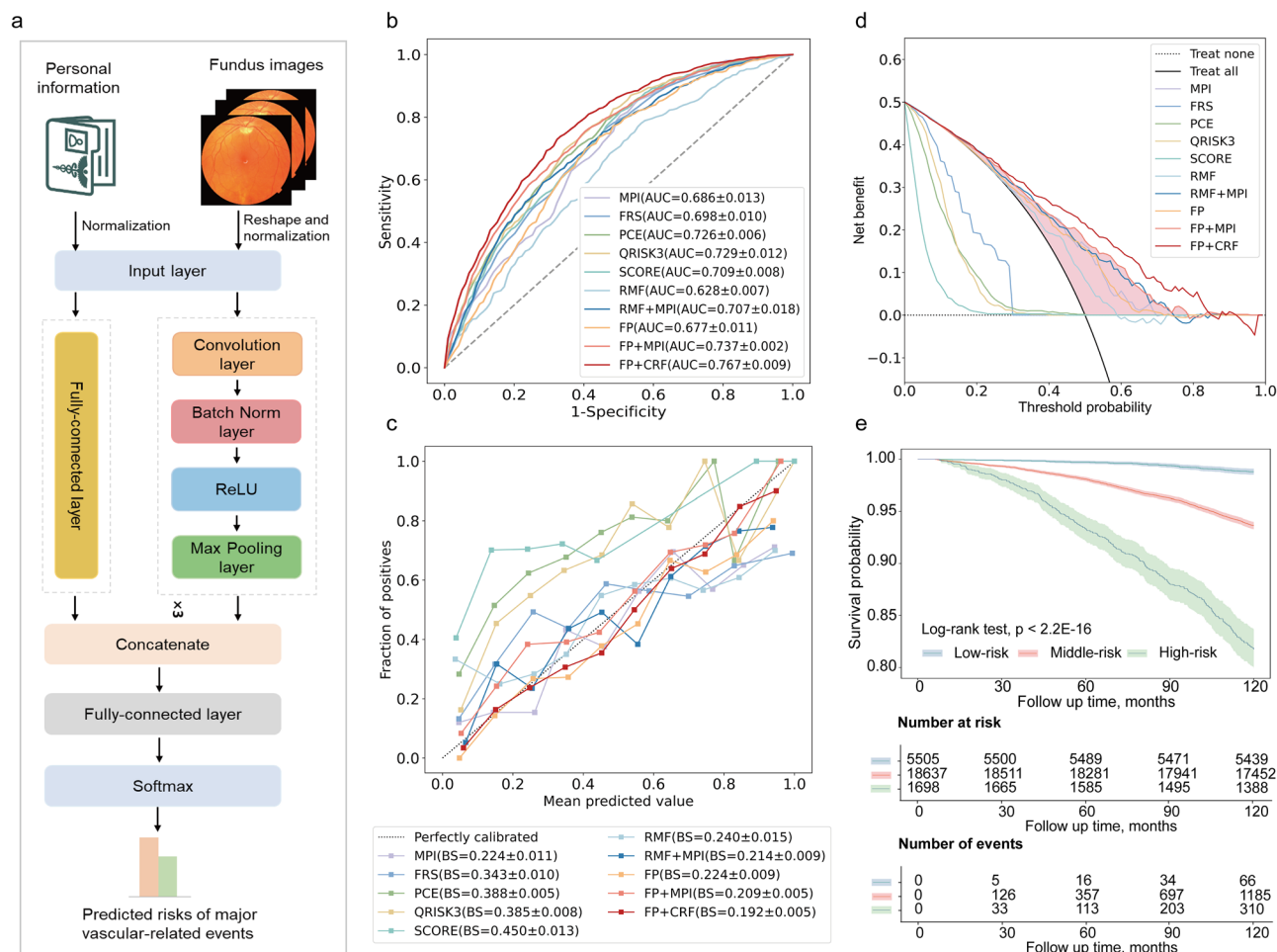


Fig. 2 | Model architecture and predictive performance. The figure illustrates the model framework and compares the predictive performance between the proposed model and baseline models. **a** Architecture of the early screening model. **b** ROC curves of the proposed model (FP + MPI), its variant (FP + CRF), and baseline models including MPI-based model, FRS, PCE, QRISK3, SCORE, RMF, RMF + MPI, and FP-based model. **c** Calibration curves. The x-axis represents the mean predicted values and the y-axis represents the fraction of positive samples. Due to the significant imbalance between positive and negative samples in the internal validation set, the calibration curve was plotted by under-sampling the negative samples

to achieve a 1:1 ratio with the positive samples, using the diagonal line as a reference. **d** Decision curves. The x-axis represents the threshold probability and the y-axis represents the net benefit. **e** Kaplan–Meier graphs for major vascular-related events in low-risk, middle-risk, and high-risk groups. AUC area under the receiver operating characteristic curve, BS Brier score, CRF clinical risk factor, FP fundus photograph, FRS Framingham risk score, MPI minimal personal information, PCE pooled cohort equation, RMF retinal microvascular features, SCORE systematic coronary risk evaluation.

Additionally, we conducted quantitative analyses of retinal microvascular features in various risk populations to identify specific vascular abnormalities in high-risk patients. Besides, we explored both the commonalities and differences in the retinal microvascular characteristics of the three vascular-related diseases, aiming to gain a comprehensive understanding of the general and specific retinal morphological changes closely associated with them. More importantly, we performed a genetic analysis on the retinal image-derived features obtained by the model to examine their potential as biomarkers and determine if there are causal effects with vascular-related diseases. The primary goal was to provide new insights and approaches for the early screening and prevention of vascular-related diseases.

Results

Characteristics of the study population

The clinical characteristics of the participants are shown in Supplementary Table 1. A cohort of 25,840 participants, with usable left eye fundus images was enrolled in the study, with a mean age of 55.21 years (SD 7.97). Over a 10-year follow-up period, 1561 individuals experienced major vascular-related events, including 354 cases of stroke, 642 cases of MI, and 672 cases of CKD. Notably, 102 individuals demonstrated multimorbidity patterns: 5

cases with concurrent stroke, MI and CKD; 16 with stroke-MI co-occurrence; 25 with stroke-CKD co-occurrence; and 56 with MI-CKD co-occurrence.

Prediction performance

Figure 2b demonstrates the predictive performance of our model in the internal validation set and provides a comparison with other benchmark models. The unimodal models achieved AUCs of 0.677 (SD, 0.011) for fundus imaging alone and 0.686 (SD, 0.013) for MPI alone. However, when enhanced MPI with retinal imaging data, the proposed model's AUC increased to 0.737 (SD, 0.002). Additionally, the model variant that incorporated both retinal imaging and additional clinical indicators demonstrated the highest predictive performance, with an AUC of 0.767 (SD, 0.009). In comparison, the widely used early screening models PCE, FRS, QRISK3, and SCORE, achieved AUC values of 0.726 (SD, 0.006), 0.698 (SD, 0.010), 0.729 (SD, 0.012), and 0.709 (SD, 0.008), respectively. The proposed models consistently demonstrated superior sensitivity and specificity compared to the baseline models (Supplementary Table 2). The probability density distribution of the predictions closely matches the actual observed event frequency on the calibration curve (BS = 0.209, SD, 0.005),

demonstrating the accuracy of the model's predictions (Fig. 2c). In contrast, the traditional risk assessment model, PCE, substantially overestimates the risk of major vascular-related events. The largest red area in the decision curve signifies a high level of accuracy and reliability of our model in decision-making capability (Fig. 2d). This implies that the model is capable of producing favorable outcomes in real-world clinical applications.

Consistency analysis in predicted probabilities based on left vs. right eyes

This study utilized fundus images from the left eye to construct a model for predicting major vascular-related events. To highlight the model's robustness in selecting fundus images, we also explored the performance of the model based on the right eye (Supplementary Fig. 1). The predictive probabilities showed a significant correlation ($R = 0.96$, $p < 2.2 \times 10^{-16}$) between the left and right eyes.

Association of predicted risks with major vascular-related events

To validate the correlation between the predicted risk of major vascular-related events and the actual occurrence of events, we categorized patients into low-risk, middle-risk, and high-risk groups based on prediction probability thresholds of 0.25 and 0.75. Subsequently, we generated Kaplan–Meier survival curves for these three groups, as illustrated in Fig. 2e. During the follow-up period, participants in the low, middle, and high-risk groups displayed significantly distinct survival outcomes (log-rank p value $< 2.2 \times 10^{-16}$). The survival curve of the low-risk group showcased the most favorable survival status, characterized by a relatively high survival rate and a stable trajectory. Out of the 5505 participants, only 66 (1.20%) experienced the adverse event. In contrast, the survival curve of the high-risk group exhibited a significant decline, indicating a heightened susceptibility to clinical events among these participants. Out of the 1698 individuals in this group, 310 (18.26%) experienced the target event, signifying a substantial increase compared to the low-risk group. This indicates a robust correlation between the predicted risk and the actual occurrence of major vascular-related events. An increasing pattern of ORs was observed in all risk groups, indicating a strong association between the predicted risks and the actual occurrence of targeted events (Supplementary Fig. 2).

Quantitative analysis of retinal microvascular features among three risk groups

To explore the correlation between retinal features and the risk of developing diseases, we performed the quantitative analysis of the retinal microvascular parameters (refer to Section “Methods”) among the high, middle, and low-risk groups (Table 1). Entire vessel maps show the full microvascular network, while artery and vein maps classify vessels as arterial or venous. All retinal features exhibit significant differences among these three risk groups ($p < 0.001$). The average width of vessels, distance tortuosity, squared curvature tortuosity, and tortuosity density exhibit a positive correlation with the increasing disease risk. Conversely, fractal dimension and vessel density exhibit smaller values in the high-risk group. Arterial and venous indicators demonstrate similar correlations. Specifically, the high-risk individuals exhibited a marked reduction in vascular branching complexity (as reflected by lower fractal dimension values in both arterioles and venules), alongside significant venular dilation (evidenced by increased retinal venular average width) and elevated vascular tortuosity (including distance-based tortuosity and squared curvature tortuosity). Furthermore, the retinal age gap in the high-risk group (4.60 (SD 4.50)) was significantly higher compared to the low-risk group (-3.74 (SD 4.53)), confirming that high-risking patients have a greater degree of microvascular aging in the eyes. The middle-risk group showed a near-neutral gap (-0.14 (SD 4.94) years), with stratified means of -1.70 ± 4.72 years (predicted probability 0.25–0.50) and 1.66 ± 4.55 years (predicted probability 0.50–0.75), demonstrating a progressive increase in retinal aging with rising predicted risk.

Subgroup analysis of three vascular-related diseases

Our model demonstrated robust performance across stroke (AUC of 0.748), MI (AUC of 0.721), and CKD (AUC of 0.752) sub-cohorts (Supplementary Fig. 3). Specifically, in the screening for CKD, our model exhibited better results compared to the eGFR-based model (AUC of 0.710). Calibration and decision curve analysis confirmed superior clinical utility across nearly all conditions. Survival curves (high/middle/low-risk groups) and retinal feature quantification consistently validated the model's predictive accuracy, aligning with primary analysis findings (Supplementary Fig. 3 and Supplementary Tables 3–5).

To improve the interpretability of our model and shed light on its diagnostic mechanism for different vascular-related diseases, integrated gradients were used to generate saliency maps to highlight valuable areas of images in corresponding subgroups. Figure 3 presents four individual saliency maps of randomly selected patients and the compiled maps. The saliency maps for three vascular-related diseases demonstrate both commonalities and differences in the model's predictive mechanisms for stroke, MI, and CKD, which are reflected by overlapping and disjoint areas of emphasis respectively. The optic disc area and the peripapillary area adjacent to major vessel branches, as well as the areas below the third branches of the temporal superior vessels, and the macula area, exhibit prominent predictive value for the model in predicting all three vascular-related diseases, suggesting a possible association between the microcirculation of the heart, brain, and kidneys and these specific regions of the retina. The saliency maps for stroke, MI, and CKD also show somewhat distinct patterns of emphasis. The model focuses more on the first and second branches of the inferior and superior temporal vessels for predicting MI compared to stroke. In the case of CKD, the model's attention is more evenly distributed throughout the retinal area, with a broader focus on microvessels and adjacent areas (the second column of Fig. 3). This effect is even more pronounced than in predicting stroke.

The quantitative analysis of retinal microvascular features in participants with three vascular-related diseases revealed both common and differential retinal morphological characteristics of stroke, MI, and CKD (Supplementary Table 6). We found that some retinal microvascular features showed no significant differences among the three vascular-related diseases, indicating partial consistency in the morphological characteristics of microvessels in retinal images. However, a few microvascular parameters did highlight significant differences. Specifically, compared to patients with stroke or CKD, patients with MI exhibited increased vessel area, fractal dimension, and vessel density. On the contrary, CKD patients showed larger average retinal microvascular width and tortuosity. The characteristics of veins and the overall binary representation of the vasculature were consistent across all three diseases. Additionally, our observations revealed differences in the degree of retinal microvascular aging among the three vascular-related diseases, with CKD patients showing the most severe aging and MI patients showing relatively less aging.

Subgroup analysis by age and sex

The model's predictive performance varied across age groups and genders. Notably, it achieved the highest accuracy in young adults (AUC = 0.721), compared to middle-aged adults (AUC = 0.674) and older adults (AUC = 0.642) (Supplementary Table 7). While all models exhibited some performance degradation in the older adult group, our proposed model and its variant (AUC of 0.673) maintained the strongest predictive capability in comparison with baseline models. Regarding gender differences, the model showed pronounced better performance in female participants (AUC of 0.760) than in males (AUC of 0.680). However, the model variant demonstrated relatively robust performance in the male subgroup (AUC of 0.735), suggesting its potential utility for gender-specific applications (Supplementary Table 8).

Sensitivity analysis

To address potential confounding by population structure, we conducted a sensitivity analysis restricted to White British participants. Both our

Table 1 | Comparison of retinal microvascular features among the high, middle, and low-risk groups

		Overall	Low-risk	Middle-risk	High-risk	p
Characteristic	Number	25,840	5505	18,637	1698	
Binary	Fractal dimension (–)	1.489 (0.035)	1.502 (0.032)	1.487 (0.034)	1.464 (0.035)	<2.22E–16
	Vessel density (–)	0.071 (0.010)	0.074 (0.010)	0.070 (0.010)	0.064 (0.010)	<2.22E–16
	Average width (pixel)	7416.400 (617.994)	7389.829 (622.269)	7417.583 (616.561)	7519.605 (607.894)	3.19E–09
	Distance tortuosity (–)	3.397 (1.189)	3.245 (1.066)	3.426 (1.206)	3.674 (1.385)	<2.22E–16
	Squared curvature tortuosity (–)	23.996 (23.416)	21.373 (20.112)	24.569 (24.138)	27.818 (25.869)	<2.22E–16
	Tortuosity density (–)	0.699 (0.034)	0.696 (0.033)	0.700 (0.034)	0.706 (0.037)	<2.22E–16
Artery	Fractal dimension (–)	1.292 (0.037)	1.305 (0.034)	1.290 (0.036)	1.266 (0.040)	<2.22E–16
	Vessel density (–)	0.030 (0.005)	0.032 (0.005)	0.030 (0.005)	0.027 (0.005)	<2.22E–16
	Average width (pixel)	7284.574 (672.663)	7333.591 (661.714)	7263.419 (674.145)	7358.619 (684.664)	2.11E–12
	Distance tortuosity (–)	5.568 (3.512)	5.202 (3.014)	5.655 (3.609)	6.009 (4.058)	<2.22E–16
	Squared curvature tortuosity (–)	72.730 (114.306)	61.280 (88.177)	75.250 (119.975)	89.182 (132.148)	<2.22E–16
	Tortuosity density (–)	0.750 (0.054)	0.747 (0.053)	0.751 (0.054)	0.754 (0.059)	7.96E–06
Vein	Fractal dimension (–)	1.315 (0.039)	1.327 (0.037)	1.313 (0.039)	1.293 (0.039)	<2.22E–16
	Vessel density (–)	0.036 (0.006)	0.037 (0.006)	0.035 (0.006)	0.033 (0.005)	<2.22E–16
	Average width (pixel)	8009.407 (790.017)	7887.956 (746.560)	8024.175 (793.901)	8350.661 (808.945)	<2.22E–16
	Distance tortuosity (–)	3.491 (1.835)	3.344 (1.637)	3.518 (1.867)	3.788 (2.153)	2.62E–14
	Squared curvature tortuosity (–)	27.271 (39.951)	25.069 (37.253)	27.730 (40.530)	30.795 (43.015)	3.49E–06
	Tortuosity density (–)	0.760 (0.042)	0.757 (0.040)	0.761 (0.042)	0.764 (0.047)	1.31E–08
Age Gap (year)		–0.593 (5.226)	–3.735 (4.531)	–0.138 (4.938)	4.597 (4.502)	<2.22E–16

– indicates that this indicator is a unitless measure.

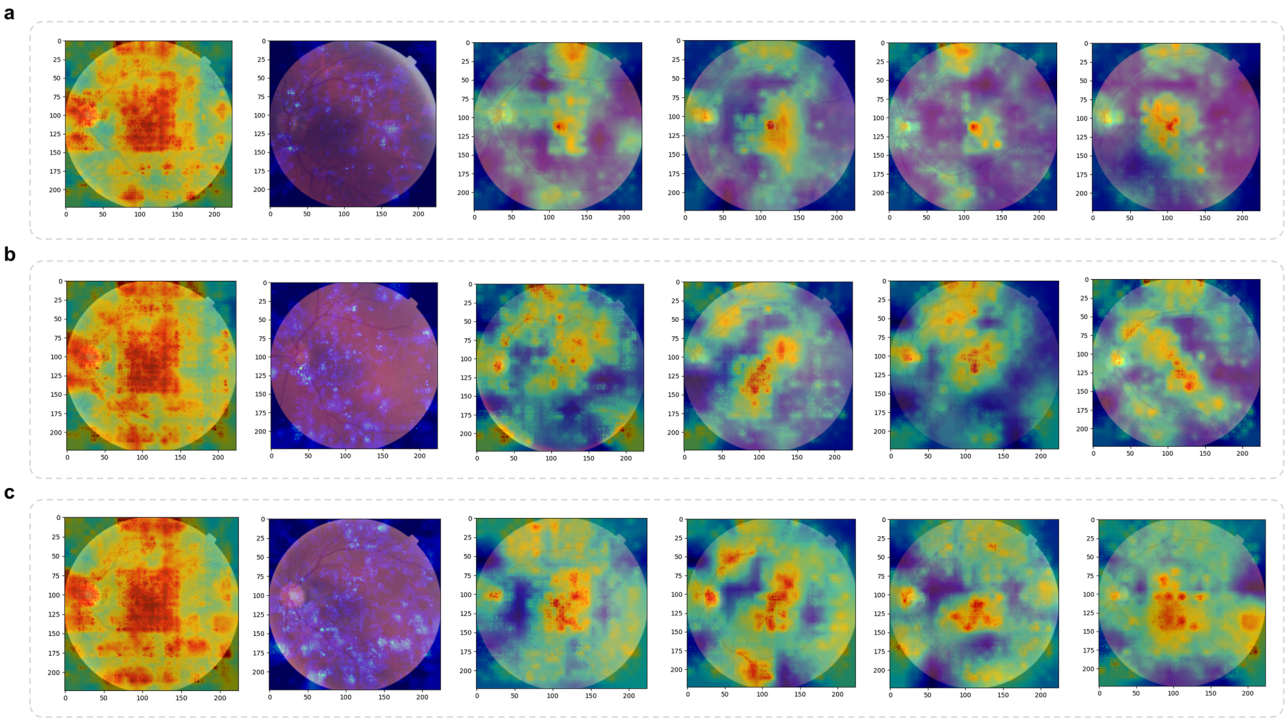


Fig. 3 | Gradient visualizations of predictions of three vascular-related diseases. This figure shows saliency maps of predictive gradients for three vascular-related diseases, highlighting clinically relevant retinal regions. **a** Stroke. **b** MI. **c** CKD. The first image presents a compiled saliency map that encompasses all patients in the subgroup. In this map, the highest value of each pixel from the saliency maps of individual patients is captured, emphasizing the distribution of retinal microvascular areas that the model considers crucial for this particular disease. The second

image shows a differential map of the compiled saliency maps for three diseases. It is a standardized representation of the first image, where brighter pixels denote that the corresponding region is more associated with the specific disease compared to the other two. The subsequent four images (3rd to 6th) exhibit saliency maps derived from fundus images of four randomly chosen patients who have the corresponding vascular-related disease.

proposed model and baseline models exhibited comparable predictive performance between the full cohort and the White British subgroup (Supplementary Table 9). Specifically, the proposed model achieved an AUC of 0.740 in the White British subgroup, closely mirroring its performance in the full cohort (AUC = 0.737; DeLong's test $p = 0.919$). Similar nonsignificant differences were observed across all baseline models (all DeLong's test $p > 0.05$), suggesting minimal evidence for population stratification effects.

Extraction of retinal image-derived traits

The 32-dimensional retinal image features obtained from the convolutional layers of the model have been reduced to 5 dimensions (retinal image-derived traits) using PCA while preserving 90% of the original feature information, namely FP_1 to FP_5. Supplementary Fig. 4 presents the t-SNE visualization results of dimensionality reduction for FP_1 to FP_5. The positive and negative samples demonstrate distinguishable patterns, indicating the potential of the identified retinal-image derived traits to effectively characterize fundus image features. Additionally, the Spearman correlation heatmap shows the relationships between these traits and retinal morphological characteristics, as well as the retinal age gap (Supplementary Fig. 5). Significant correlations (marked with asterisks) are observed across various features, highlighting the association between specific retinal image traits and morphological characteristics. For instance, FP_1 exhibits a significant inverse correlation with the average width of arteries and veins. FP_2 shows a significant negative correlation with the fractal dimension and vascular density of the retinal microvasculature, while it has a significant positive correlation with the average width. FP_3 is significantly positively correlated with fractal dimension and vascular density. FP_4, compared to other traits, demonstrates a stronger positive correlation with the fractal dimension and vascular density of the fundus microvasculature.

Genetic analysis of retinal image-derived traits

GWASs for 5 retinal image-derived features identified a total of 24 genome-wide-significant ($p < 1.0 \times 10^{-8}$) loci (Fig. 4 and Supplementary Data 1). Genomic heritability was estimated at 9.9% (SE, 2.4%), 4.6% (SE, 1.9%), 17.8% (SE, 2.6%), 8.7% (SE, 2.3%), 6.8% (SE, 2.1%) for 5 retinal image-derived traits. The average SNP-based heritability was 9.56%. According to the GeneCards database, 10 out of the 119 mapped genes obtained from FUMA are involved in various biological functions, including brain regulation (SRRT), kidney function (PLEKHA6, DSTYK), blood vessel development (EPHB4, SLC12A9, CHEK1, PDE3A, NOX4), and regulation of vascular functions (PLCB1, PLCB4). By querying the GWAS Catalog, we found that the identified loci affect a diverse range of traits (Supplementary Data 2). In addition to retinal microvascular characteristics such as vascular fractal density and vascular fractal dimension, these loci are also associated with clinical biomarkers linked to vascular-related diseases, such as eGFR, high-density lipoprotein cholesterol levels, and cystatin C levels.

Significant genetic correlation between retinal image-derived traits was only observed in a few traits, including FP_1 and FP_4 ($rg = -0.43$), as well as FP_3 and FP_4 ($rg = -0.30$, Supplementary Table 10). Additionally, we analyzed the genetic correlations between retinal image-derived traits and retinal microvascular features using available summary statistics from eight GWAS datasets (Supplementary Table 11). Although most retinal image-derived traits showed significant phenotypic associations with retinal microvascular parameters, only a few exhibited significant genetic correlations after FDR correction. Specifically, significant genetic correlations were observed only with vessel density, whereas no significant associations were found with vessel width or tortuosity. In contrast, colocalization analysis revealed stronger evidence of shared genetic basis between retinal image-derived traits and retinal microvascular features (Supplementary Table 12). With the exception of FP_2, nearly all retinal image-derived traits shared genetic variants with all available retinal microvascular traits. FP_2 showed shared variants only with fundus microvascular tortuosity and vessel density, but not with vessel width.

Genetic analyses of retinal image-derived traits and three major vascular-related diseases revealed potential shared genetic basis. Our analysis identified significant genetic correlations between FP_2 and both stroke and CKD, as well as between FP_3 and both stroke and MI (Fig. 5a). However, no significant genetic associations were observed between other retinal traits and these three diseases. Colocalization analysis further uncovered additional shared genetic foundations. Nearly all retinal image-derived traits exhibited colocalized genetic loci with the three vascular-related diseases (Supplementary Table 13). For instance, FP_1 colocalized with stroke at SNP rs12913832 (Fig. 5b, PPH4 = 0.99), FP_2 colocalized with CKD at SNP rs12913832 (Fig. 5c, PPH4 = 0.99), and FP_3 colocalized with MI at SNP rs1800407 (Fig. 5d, PPH4 = 1.00).

Causal effects between retinal image-derived traits and major vascular-related diseases

We conducted a systematic analysis using two-sample bidirectional MR to examine the causal relationship and effects between five retinal image-derived traits and three vascular-related diseases, i.e., stroke, MI, and CKD. Expect for a few IVs groups that exhibited heterogeneity and pleiotropy, sensitivity analysis found no evidence of confounding heterogeneity of effect sizes (Cochran Q statistic, $p > 0.001$; Supplementary Tables 14 and 16) or from pleiotropy (MR-Egger intercept, $p > 0.05$; Supplementary Tables 15 and 17). In the forward MR analysis, where retinal image-derived traits were treated as exposures, we found nominally significant causal effects for stroke with FP_1 as well as FP_2, and for MI with FP_4 and FP_5 (Supplementary Tables 18 and 19). However, after applying the FDR correction, only the preceding findings remained significant ($p = 0.003$, FDR-corrected $p = 0.043$ for FP_1; $p = 0.006$, FDR-corrected $p = 0.046$ for FP_2; Fig. 5e). In the reverse MR analysis, where the three vascular-related diseases were considered exposures, we observed nominally significant causal effects for CKD with FP_2, FP_3, FP_4, as well as FP_5, and only the effect with FP_2 passed the FDR correction ($p = 0.002$, FDR-corrected $p = 0.026$; Fig. 5e). These findings suggest that changes in retinal image-derived traits may have a noticeable impact on the risk of stroke and MI, while CKD may potentially act as a contributing factor to retinal microcirculation.

External temporal validation

The clinical characteristics of the validation cohort are presented in Supplementary Table 20. An independent cohort of 4558 participants with usable left-eye fundus images was enrolled for external temporal validation, with a mean age of 59.42 years (SD 7.78). Over a 10-year follow-up period, 350 individuals experienced major vascular-related events, including 75 cases of stroke, 141 cases of MI, and 159 cases of CKD. Among these, 1 patient presented with concurrent stroke, MI, and CKD; 6 exhibited stroke-MI co-occurrence; 5 had stroke-CKD co-occurrence; and 12 displayed MI-CKD co-occurrence.

The results from this cohort confirm the generalizability of our model to new populations, showcasing superior performance compared to traditional risk assessment models (Supplementary Fig. 6). For composite major vascular-related events, the AUC of the proposed model was 0.732, reflecting improvements of 4%, 1.8%, 0.9%, and 3.7% over FRS, PCE, QRISK3, and SCORE, respectively. When compared to RMF-based approaches, our model maintained this performance advantage, showing absolute AUC increases of 7% and 2% against the RMF-only and RMF + MPI models, respectively. In sub-cohorts, the model demonstrated superior performance, except for stroke, with a particularly notable improvement in the FP + CRF model variant. Sensitivity and specificity further highlighted the model's superiority to identify high-risk individuals (Supplementary Table 21). Additionally, calibration and decision curves provided further support for the model's superiority in this new cohort.

Our stratified evaluation revealed nuanced performance patterns across demographic subgroups. Diverging from primary analyses, the proposed model demonstrated superior predictive performance in middle-aged adults (AUC of 0.703) compared to both younger and older adult subgroups within the validation cohort (Supplementary Table 22). Notably,

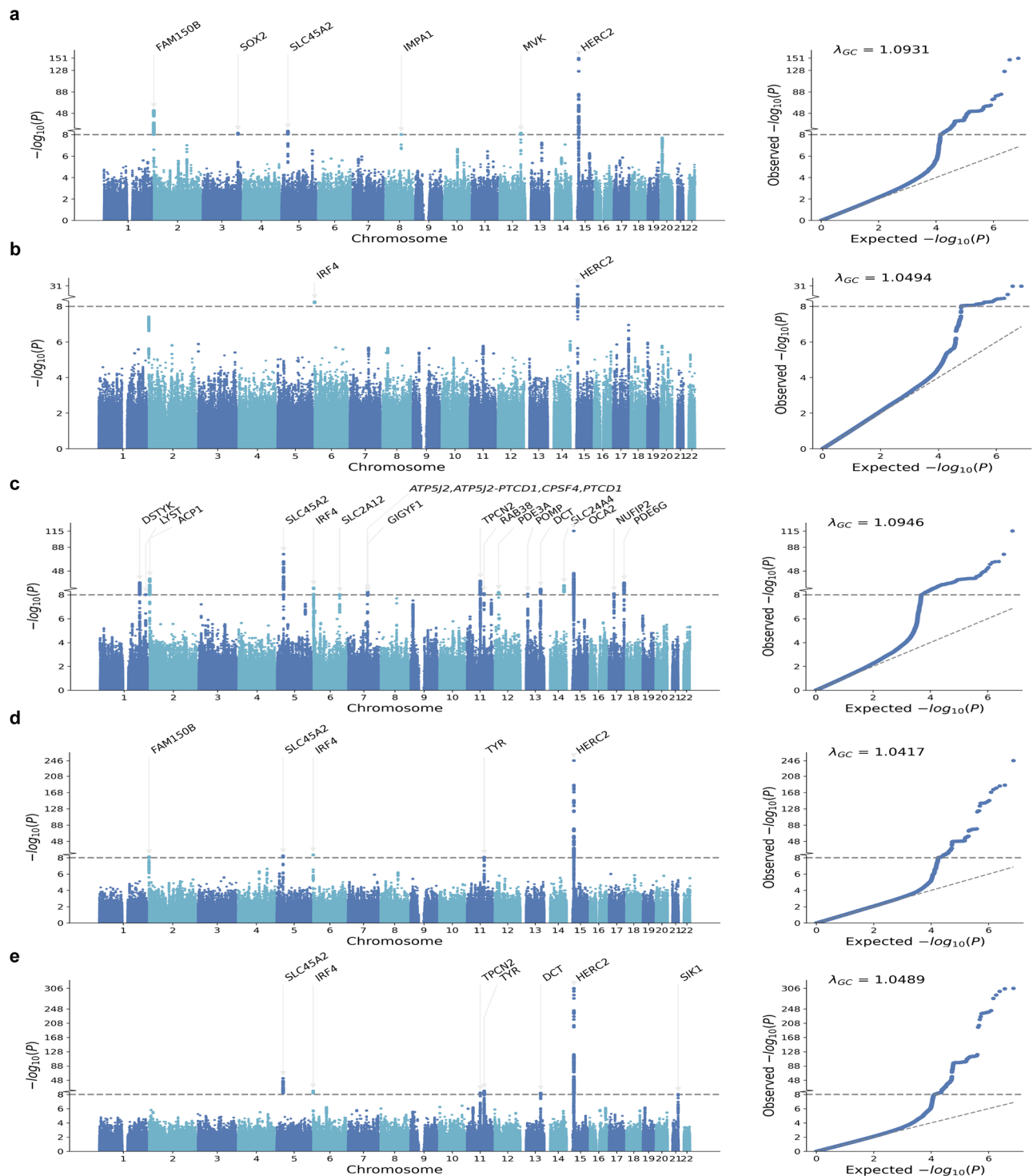


Fig. 4 | GWAS analysis of retinal image-derived traits. This figure presents Manhattan and QQ plots visualizing the genome-wide association results for FP_1 (a), FP_2 (b), FP_3 (c), FP_4 (d), and FP_5 (e).

the model maintained its performance advantage over baseline approaches specifically in middle-aged and older populations. Sex-specific analyses corroborated primary findings (Supplementary Table 23), with consistently stronger prediction accuracy in females (AUC of 0.770) versus males (AUC of 0.684).

Discussion

In this study, we examined the correlation between retinal microcirculation and major vascular-related diseases from both phenotypic and genetic

perspectives. Phenotypically, we proposed a deep learning model for the early screening of major vascular-related diseases using fundus images. Instead of screening different diseases separately, we integrated representative vascular-related diseases into a single model. We demonstrated that the deep learning model, integrating accessible fundus images and MPI, could achieve superior and promising performance for major vascular-related events when compared to traditional assessment models. Through further quantitative analysis, we identified the retinal morphological features associated with high-risk patients for major vascular-related diseases,

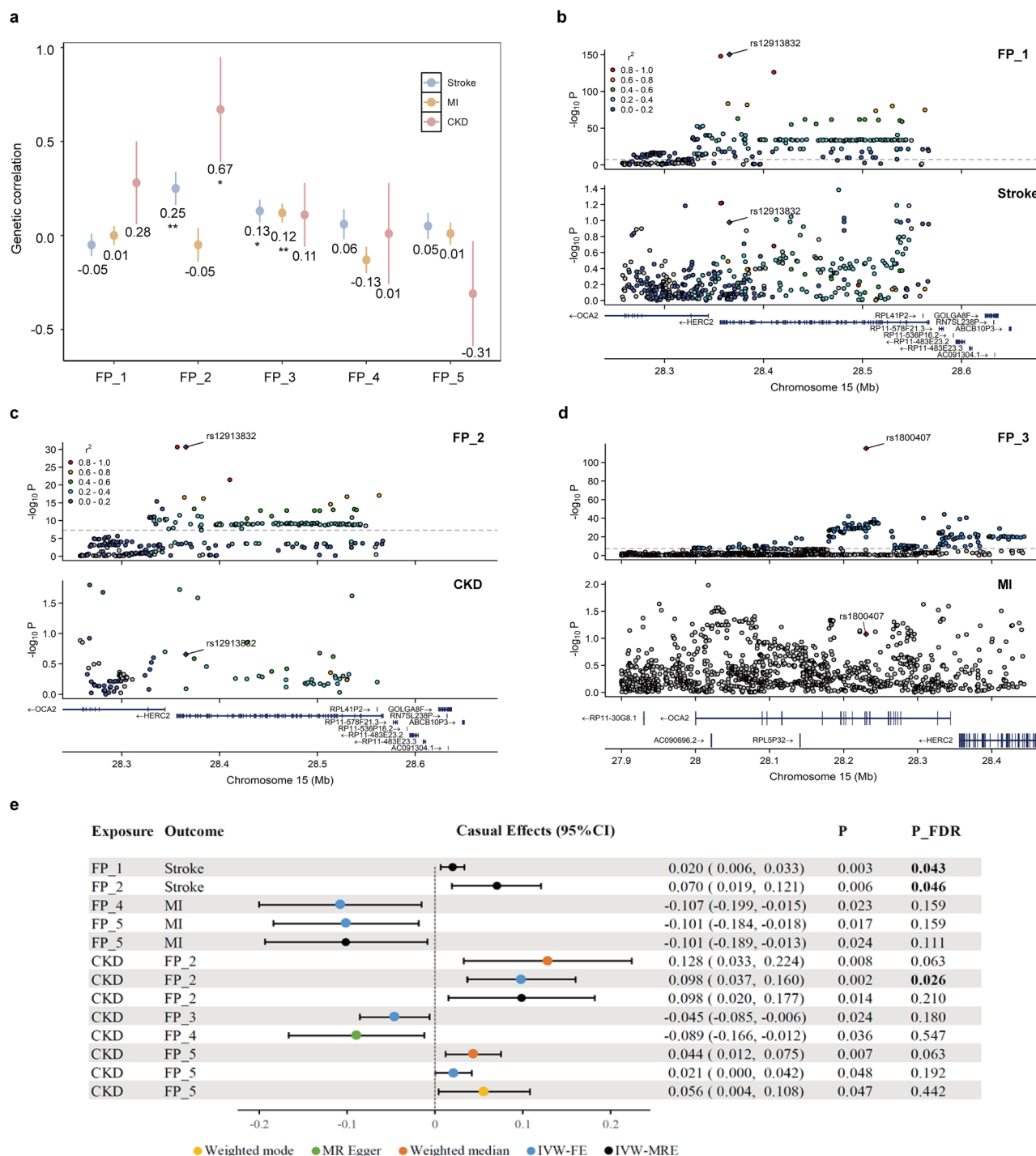


Fig. 5 | Genetic associations and causal effects between retinal image-derived traits and three vascular-related diseases. The figure presents genetic correlations, colocalization results, and causal relationships between retinal image-derived traits and stroke, MI, and CKD. **a** Genetic correlations between retinal image-derived traits and stroke, MI, and CKD. Results that passed the significant threshold (FDR-adjusted $p < 0.05$) were marked in the plot. FDR-adjusted p values of <0.001 , <0.01 ,

and <0.05 are indicated as ***, **, and *, respectively. **b** Colocalization results between FP_1 and stroke. **c** Colocalization results between FP_2 and CKD. **d** Colocalization results between FP_3 and MI. **e** Significant causal effects ($p < 0.05$) in bidirectional MR results, with significant FDR-adjusted p values in bold. CKD chronic kidney disease, FDR False Discovery Rate, FP fundus photograph, MI myocardial infarction.

as well as patients within different disease groups. Genetically, our study revealed the potential of using extracted retinal image-derived features as biomarkers and suggested a causal relationship between retinal micro-circulation and major vascular-related diseases.

Previous studies have endeavored to predict vascular-related diseases, along with their associated risk factors, utilizing retinal fundus images^{14,30,38,39} and optical coherence tomography (OCT) scans^{40–42}. These investigations

have not only affirmed the efficacy of early screening models but have also underscored the feasibility of this technological pathway. However, most existing models based on fundus images predominantly concentrate on screening for a particular disease. In essence, these proposed models are only effective in a narrow range of early screening scenarios. It is more efficient in clinical practice to employ a comprehensive screening model that encompasses multiple crucial vascular-related diseases, as opposed to a single-

disease screening model³². Physiologically, the retinal microcirculation is an integral part of the systemic microcirculation, interrelated with the microcirculation of vital organs such as the heart, brain, and kidneys^{13,43}. Correspondingly, conditions such as MI, stroke, and CKD are significant contributors to mortality and socioeconomic burden worldwide^{3,14}. By targeting the composite events related to these three representative diseases in our prediction model, we demonstrated its practicality and potential to enhance disease screening efficiency, particularly in scenarios involving large-scale screening and limited medical resources.

Existing studies have utilized retinal imaging to predict various vascular diseases, although their performance varies to some extent. In the study focused on major adverse cardiac events, an AUC score of 0.73 (SD 0.04) was achieved, showcasing comparable predictive ability with our study³⁹. A similar level of performance was observed in the study aiming to predict coronary artery calcium, where an AUC score of 0.742 (95% CI 0.732–0.753) indicated promising predictive potential². In another study focused on retinal imaging-based prediction of MI, they achieved an AUC score of 0.80 (SD 0.02), surpassing the AUC score of our model¹⁴. This may be attributed to the incorporation of a comprehensive range of clinical indicators in their model, including gender, age, HbA1c, systolic and diastolic blood pressure, smoking habit, alcohol consumption, glucose, and body mass index, which may enhance their predictive performance. Furthermore, a study focused on diagnosing cardiovascular diseases using retinal imaging and reported an impressive AUC score of 0.872 (95% CI 0.857–0.886)³⁸. One possible reason for this could be that they included various risk factors such as systolic blood pressure, total and high-density lipoprotein cholesterol, and hypertension. It is worth noting that the diagnosis of cardiovascular diseases is generally considered easier compared to predicting the risk over a 10-year period. In contrast to these studies, our model adopts a more streamlined approach by solely considering minimal demographic information, specifically age and gender. These easily obtainable indicators not only simplify the process but also hold the advantage of non-invasiveness, eliminating the need for any intrusive procedures. We also observed pronounced age and gender disparities in the predictive performance of the proposed model. Specifically, the model showed superior performance in women compared to men. This finding aligns with previous studies that have also reported gender differences in predicting vascular-related events^{21,44}. For instance, studies by Liew et al.⁴⁵ and Wong et al.⁴⁶ found that changes in retinal vessel characteristics were associated with an increased risk of vascular diseases in women, but not in men. A meta-analysis focusing on retinal vessel caliber and risk for coronary heart disease also highlighted an association between retinal vessel changes and increased risk in females, but not in males²¹. These findings indicate significant differences in microcirculation between males and females, suggesting that retinal microvasculature may serve as a more effective indicator of vascular health in women than in men.

The populations identified as high-risk and low-risk based on the model screening exhibit significant distinctions in all retinal parameters, signifying a correlation between retinal microvascular features and the likelihood of developing major vascular-related diseases. Notably, we found that the high-risk individuals exhibited a marked reduction in vascular branching complexity, alongside significant venular dilation and elevated vascular tortuosity. Existing studies have confirmed that reduced fractal dimension may indicate higher risks for various health issues such as stroke, incident mortality, hypertension, congestive heart failure, and renal failure, which is consistent with our main findings^{23,24,47}. Likewise, researchers have suggested that lower retinal vascular density is associated with a high AHA (American Heart Association) risk score, hypertension, congestive heart failure, and renal failure, which aligns with our study's results^{24,48}. Previous studies have consistently found a significant connection between higher retinal vascular tortuosity and an increased prevalence of cardiovascular diseases⁴⁹. Our study's results reinforce this link, highlighting the importance of retinal vascular tortuosity as a clinical marker for identifying individuals at risk. Retinal age gap, a novel biomarker to evaluate the aging of microvascular status, has been convincingly demonstrated to have a robust

correlation with the occurrence of multiple diseases, such as stroke, arterial stiffness, incident cardiovascular disease, and kidney failure^{50–52}. A positive retinal age gap indicated an “older”-appearing retina, while a negative one indicated a “younger”-appearing retina. Remarkably, our study has yielded results consistent with prior research, revealing a substantial escalation in retinal vascular aging among high-risk patients susceptible to severe vascular ailments.

In addition to evaluating the all-cause predictive performance of the proposed model, we conducted a thorough analysis of its direct application in predicting the three target vascular-related diseases. Notably, the saliency maps revealing the model's prediction mechanisms highlight a significant portion of the retina, indicating the strong correlation between retinal microcirculation and the microcirculation of the heart, brain, and kidneys. In the aggregated maps, the optic disc area and the peripapillary area adjacent to major vessel branches, as well as the areas below the third branches of the temporal superior vessels, and the macula area, are the primary areas of interest, suggesting a close association between these locations and the occurrence of outcome events. Despite the absence of retinal microvessels in the macular region, the model places significant emphasis on this area. This could be attributed to the presence of a dense network of blood vessels in the surrounding retina of the macula, and the possibility that morphological alterations in these microvessels are closely interrelated with major vascular-related diseases. Additionally, there may exist a correlation between other retinal ailments and the occurrence of vascular-related diseases^{53,54}. Previous studies utilized saliency maps to investigate the predictive mechanisms of the models based on fundus images in predicting CKD, cardiovascular disease, and other conditions^{28,30,38}. They discovered that the highlighted regions were primarily located in the optic nerve, central macula, vessel branch points, and arterial-venous junctions, which align with the important retinal regions identified in our study. In addition to confirming the significance of the main vascular trunk in providing valuable information, our research also underscores the correlation between the third branches of the temporal superior vessels and their impact on the outcome. This additional finding serves as a valuable supplement to the existing body of research. Although the primary regions of interest align across the diseases, it is particularly significant to note that CKD demonstrates a wider focus on retinal areas compared to the other two diseases. This intriguing observation suggests a potential link between the occurrence of CKD and subtle microvascular alterations within the retina.

We conducted a comparative study on the retinal morphological features of the three vascular-related diseases to identify associations between retinal microcirculation and the risk of these diseases. To the best of our knowledge, this investigation had not been previously undertaken. The results we obtained revealed distinctive differences in the retinal pathology between different vascular-related diseases, despite the heart, brain, and kidneys all being part of the systemic microcirculation. Specifically, patients at risk of developing CKD exhibited lower fractal dimension and vessel density, as well as higher average vessel width and tortuosity density, which closely resemble the morphological characteristics observed in high-risk populations. Notably, the disparities in microvascular parameters of veins were more significant among the three diseases, aligning with the overall binary vessel analysis results. In addition, the significant differences in the retinal age gap across these three vascular-related diseases provide valuable insights for assessing the acute and chronic nature of vascular events. Individuals at risk of MI exhibit the smallest difference in retinal aging, signifying a milder degree of microvascular aging and implying a swifter onset of MI. Conversely, patients at risk of CKD display the largest retinal age gap, indicating a more advanced stage of vascular aging and suggesting a slower progression of this condition. These findings are highly significant in advancing the understanding of the retinal morphological mechanisms of major vascular-related diseases and their clinical management.

As mentioned earlier, previous studies have yielded favorable results in using fundus images to screen for various diseases^{14,30,49,55}. However, these studies primarily prioritize the development of screening models, and their

impressive predictive performance merely showcased the phenotypic correlation between retinal microcirculation and diseases. They did not delve into the genetic relationship or causal effects, thus lacking the necessary chain of evidence. In this study, we not only examined the phenotypic correlation between retinal microcirculation and diseases but also investigated their genetic relationship and causal effects. The results of the GWAS analysis confirmed that the extracted retinal image-derived features could serve as potential biomarkers for major vascular-related diseases, consistent with prior genetic findings from retinal OCT imaging studies⁵⁶. Genetic analysis of retinal image-derived traits in relation to the three vascular-related diseases revealed shared variants, thereby suggesting a common genetic basis between retinal microcirculation and microcirculation in the heart, brain, and kidney. This finding provides new insights for further exploration of the genetic mechanisms underlying these major vascular-related diseases. We also found that the significant loci identified for retinal image-derived traits simultaneously influence risk factors for vascular-related diseases, such as BMI^{57–59}, and smoking initiation^{60,61}, and biomarkers for vascular-related diseases such as blood pressure²⁵, estimated glomerular filtration rate^{62–64}, high-density lipoprotein cholesterol levels^{65–67}, serum creatinine levels⁶⁷, and blood urea nitrogen levels^{62,63,67}. This finding suggests that the utilization of retinal images for predicting major vascular-related diseases may involve leveraging the prediction of risk factors and biomarkers. In addition, the loci of retinal features identified in this study overlap with previously identified retinal biomarkers like retinal fractal dimension and vessel density²⁴. These findings further support the potential of the extracted retinal image-derived features to serve as an objective measure for retinal vasculature.

The MR analysis results offer additional insights, indicating the potential causal relationship between retinal microcirculation and major vascular-related diseases. It is worth noting that the causal effects between retinal characteristics and these three vascular-related diseases have distinct natures. Specifically, changes in retinal microvasculature occur prior to the onset of stroke and MI, whereas the manifestation of renal vascular disease may cause modifications to retinal characteristics. These variations potentially reflect discrete mechanisms underlying the onset and progression of stroke, MI, and CKD. One potential explanation for the divergence of CKD from the other two diseases is that it predominantly affects small microvessels, causing a gradual onset and protracted disease course^{68,69}. The initial renal impairment in CKD causes changes in vascular structure and function, ultimately leading to modifications to the retinal microvasculature⁷⁰. In contrast, MI and stroke manifest more acutely and are primarily linked to greater vessels like major arteries and coronary arteries⁷¹. The changes in retinal microvasculature in conjunction with systemic vascular alterations are the primary factors behind the occurrence of these events. These findings highlight the likely causal link between retinal microvasculature and acute vascular events, thereby potentially identifying a new causal risk factor for retinal microvascular abnormalities that may be used for monitoring and therapeutic modulation. Besides, the order in which events occur, as determined by their causal relationships (i.e., CKD preceding retinal microvascular changes, and retinal microvascular changes preceding stroke and MI) is consistent with previous studies indicating that CKD is a risk factor for cardiovascular events^{34,72}. Additionally, it can be observed that the causal impact of retinal image-derived features on MI and stroke is not as robust as the inverse causal effect. This could be attributed to the fact that the retinal microvasculature predominantly consists of microvessels, and the homogeneity with the small vessels involved in CKD is significantly stronger than that with the great vessels involved in MI and stroke⁶⁸. Regarding the MR analysis, we recognize the complexity of establishing causality, especially when examining the occurrence of vascular diseases. While MR provides useful insights into the potential causal relationships, we emphasize the need for cautious interpretation of the results. The observed associations may reflect underlying systemic processes rather than direct causality. Our findings suggest that retinal microvascular changes could serve as early markers of vascular health, but further research is needed to confirm the causal direction and understand the underlying mechanisms.

The potential bidirectional nature of these relationships—where retinal abnormalities may both influence and be influenced by vascular disease—requires further exploration.

Overall, while numerous studies have utilized retinal imaging for vascular disease screening, our research presents several key advancements. First, we integrate both phenotypic and genetic analyses, offering a more comprehensive understanding of the relationship between retinal microcirculation and vascular diseases. Second, whereas many studies focus on individual vascular conditions, our model expands the scope to include vascular diseases affecting the heart, brain, and kidneys, providing a more integrated approach to vascular health. Third, we go beyond qualitative assessments by quantitatively analyzing retinal microvascular features, providing more precise insights into early markers associated with vascular diseases. Finally, through genetic analysis using GWAS and Mendelian randomization, we not only identify associations but also uncover potential causal relationships, thereby deepening our understanding of the underlying mechanisms driving vascular diseases.

We also acknowledge limitations. Several limitations should be considered. First, the relatively small sample size, particularly regarding the number of positive cases, may introduce potential bias. Expanding the sample size would improve the robustness and generalizability of our findings. Second, demographic biases within the UK Biobank, such as age, ethnicity, and social class, could limit the broader applicability of our results. Future studies incorporating more diverse cohorts are needed to enhance generalizability. Third, model validation was conducted using external temporal validation within the UK Biobank cohort, focusing on participants who had undergone the first repeat assessment visit. While this cohort is independent, future validation with larger, more diverse samples from multiple datasets will be important for a more comprehensive assessment of the model's generalizability. Fourth, although the proposed model demonstrates promising AUC values (0.74–0.77), further refinement is necessary to achieve the level of discrimination required for clinical use, potentially through feature expansion, model optimization, or by incorporating more diverse or higher-quality data. Additionally, while image quality assessment was incorporated in our analysis, we did not specifically account for potential confounding factors such as refractive errors and axial length measurements. These unmeasured variables might have influenced the imaging outcomes and therefore warrant consideration in future investigations. Furthermore, while we have sought to explore both phenotypic and genetic associations between retinal image-derived traits and retinal microvascular features, their exact biological significance remains unclear, owing to the constraints imposed by PCA-based dimensionality reduction. These traits should be considered primarily as proxies for investigating the relationship between retinal images and major vascular-related diseases. Future studies should focus on identifying more meaningful retinal image traits to improve biological interpretability and clinical relevance. Moreover, the deep learning model used in our study, while effective, remains a black-box, and its interpretability is limited. The lack of transparency in model decisions may hinder its clinical acceptance and application. Future work should aim to enhance model explainability, potentially by integrating more interpretable methods or by exploring causal relationships in greater depth. Finally, our study did not examine the potential associations between retinal microvascular features and other omics data, such as metabolomics or proteomics. Incorporating such data in future studies could provide valuable insights into the underlying molecular mechanisms.

Our study should be interpreted in light of its potential clinical impact. First, we developed a robust and efficient screening model that leverages retinal images and minimal demographic data to assess the 10-year risk of major vascular-related diseases. With increasing accessibility to retinal photography in community and primary care settings, our model holds promise as a practical tool for early identification and primary prevention of cardiovascular events, offering a non-invasive and cost-effective means for clinicians to detect at-risk individuals in settings such as primary care clinics, community health centers, and ophthalmology practices. Second, our research identified distinct retinal morphological features associated with

high-risk individuals and patients with various vascular-related diseases. These features serve as reliable, interpretable biomarkers for early detection, enabling healthcare providers to make more informed, data-driven decisions about preventive care. By recognizing these features, clinicians can tailor interventions based on individual risk profiles, ultimately improving the effectiveness of prevention strategies. Third, our genetic analysis of retinal image features has uncovered their potential as biomarkers of genetic susceptibility. The causal links between retinal microcirculation and vascular-related diseases provide valuable insights into their pathophysiology, guiding clinicians in identifying patients at higher genetic risk and informing future therapeutic strategies. In conclusion, this study highlights the strong association between retinal microcirculation and major vascular-related diseases from both phenotypic and genetic perspectives. The deep learning-based retinal image prediction model offers clinicians a powerful, scalable tool to predict major vascular events up to 10 years after a retinal examination. By facilitating earlier detection and supporting more personalized prevention efforts, this model has the potential to significantly improve patient outcomes and optimize clinical decision-making.

Methods

Datasets and subjects

Our study utilized data obtained from the UK Biobank (UKB) study, which enrolled around half a million individuals from 2006 to 2010 (<https://www.ukbiobank.ac.uk/>). The study was approved by the North West Multi-centre Research Ethics Committee, the National Information Management Board, and the UK government. The ethical considerations for research involving individuals were thoroughly reviewed, and participants provided written informed consent. As part of the eye assessments conducted during participants' visits to the UKB assessment center, retinal imaging scans were performed. We obtained all retinal fundus images from Category 100,016. In order to enhance the operability of the early screening model and streamline the screening process, we simplified the necessary personal information to only collect age and gender, making it more practical and accessible for primary medical and health care institutions and ophthalmology clinics. To compare with traditional risk assessment models, a combination of variables derived from the participant's history and blood samples—such as systolic and diastolic blood pressure, smoking habit, total cholesterol, high-density lipoprotein cholesterol, and history of hypertension—were also collected.

Participants who had retinal imaging scans during their initial assessment visits (2006–2010) were included in this study. We excluded participants with serious eye conditions such as glaucoma, trauma, diabetic retinopathy, or macular degeneration based on their diagnostic records, as these conditions had the potential to cause alterations in the retinal fundus image^{14,73}. Participants who were diagnosed with any of the major vascular-related diseases including stroke, MI, or CKD prior to the baseline, as determined by the time of retinal imaging acquisition, were also excluded from the study. The inclusion and exclusion criteria for participants are reported in Supplementary Fig. 7.

Image preprocessing

Retinal photographs of the optic disc and macular were taken at baseline for both eyes using a Topcon 3D OCT-1000 Mark II system. The system has a 45° field angle, scanning range of 6 mm × 6 mm centered on the fovea, acquisition speed of 18,000 A-scans per second⁷⁴. The images were converted to JPEG and resized to 224 × 224 pixels for input into the neural network with center cropping. During the training phase, data augmentation techniques such as random horizontal and vertical flipping, random rotation within 30 degrees, random brightness adjustment with a factor of 0.1, and random zoom with a factor of 0.1 were applied as data augmentation to facilitate improved and generalized network learning.

In accordance with prior studies, a deep learning method was employed to assess the quality of retinal images, ensuring that they met certain pre-specified criteria of sufficient quality while filtering out images with poor clarity, low contrast, and significant artifacts^{14,75}. This assessment

method utilized the publicly available EyePACS dataset (<https://www.kaggle.com/c/diabetic-retinopathy-detection/data>) to train and validate its performance^{14,76}. Any retinal fundus images classified as “reject” during the quality assessment process were excluded from further analysis, while the remaining images were used for both model training and validation. This selection process was verified by the collaborating ophthalmologist, who randomly sampled and manually confirmed the retained retinal images.

We also utilized pre-existing retinal imaging feature extraction tools to obtain meaningful retinal microvascular features (RMF)^{24,77}. Specifically, the extracted parameters included fractal dimension, vessel density, average width, distance tortuosity, squared curvature tortuosity, and tortuosity density of whole binary vessels, as well as arteries and veins. It is worth noting that distance tortuosity, squared curvature tortuosity, and tortuosity density are specific parameters used to quantify the degree of blood vessel tortuosity, albeit calculated using different calculation methods. To measure the extent of retinal vascular aging, we calculated the retinal age gap based on previous studies, with a larger value indicating more severe vascular aging^{24,50}.

Definition of major vascular-related events

In this study, major vascular-related events are defined as a composite outcome encompassing stroke, MI, and CKD. During a 10-year follow-up period, the occurrence of any one of these three diseases is considered indicative of experiencing the major vascular-related event. The identification of these cases was achieved through linkage to electronic health records, which encompassed admissions and diagnoses from hospitals in England, Scotland, and Wales, as well as information on the cause of death obtained from national death registers. Stroke and MI were ascertained by the UK Biobank Outcome Adjudication Group, utilizing specific diagnostic codes from both the 9th edition of the International Classification of Diseases (ICD-9) and ICD-10. The incidence of CKD was determined based on the codes from the ICD-10 and the Office of Population Censuses and Surveys Classification of Interventions and Procedures version 4 (OPCS-4)²⁸. The specific codes corresponding to the disease definitions can be found in Supplementary Table 24. The follow-up period commenced from the date of retinal image acquisition and concluded upon death, diagnosis of major vascular-related events, or the end of the follow-up period, whichever came first.

Model development and training

We utilized a multimodal deep learning approach, which utilizes multiple data sources to train networks (Fig. 1a). Specifically, we conducted a multimodal network by integrating a convolutional neural network (CNN) for FP and a deep neural network (DNN) for MPI (Fig. 2a). To extract features from retinal images, we developed a three-layer CNN that was specifically designed for this purpose. Instead of using well-established pre-trained models like ResNet-50 or DenseNet-169^{78,79}, we chose not to employ them due to preliminary experiments showing significant overfitting issues and subsequent decline in model performance. Meanwhile, we utilized a DNN to capture the nonlinear interactions among MPI (age and gender). The network had one fully connected layer followed by a rectified linear unit. The weights of the networks were randomly initialized. These two separate networks were then concatenated into a fully-connected layer for multi-modality feature fusion. The final layer with a *Softmax* function was appended to predict the major vascular-related events. To enhance the predictive performance of the model without considering the ease of data acquisition, we further developed a variant that incorporates additional clinical risk factors (CRF). This variant includes clinical indicators such as total cholesterol, high-density lipoprotein, and systolic blood pressure, as used by PCE.

The cross-entropy loss was used as an objective function for the classification task. The models were trained using back-propagation of errors in batches of 16 images resized to 224 × 224 pixels for 200 epochs with a learning rate of 5.0E−04. To prevent overfitting, we employed an early stopping strategy whereby the model training would stop if the

loss on the validation set did not decrease for 20 consecutive epochs. In order to address the severe class imbalance in the data where negative examples outweigh positive ones, we applied a strategy combining the SMOTE algorithm to oversample the positive examples with an undersampling technique to handle the negative examples⁸⁰. Additionally, we utilized a five-fold cross-validation approach to alleviate the random error introduced by data selection. The models were implemented using PyTorch.

Performance comparison between the proposed model and baseline models

The performance of the early screening model proposed in this study was compared to that of baseline models, including models based solely on MPI and FP, traditional risk assessment models, and RMF-based models (Fig. 1b). To the best of our knowledge, there is a gap in risk assessment models that can effectively screen for 10-year risks of stroke, MI, and CKD simultaneously. For comparison, we selected the PCE, FRS, QRISK3, and SCORE models, which are extensively applied in clinical settings to evaluate the 10-year risk of cardiovascular and cerebrovascular diseases. Notably, previous studies have also confirmed the usability of these models in screening for CKD^{16,81,82}. In addition, we also incorporated logistic regression-based predictive models based on RMF as baselines, including RMF alone and RMF + MPI. Furthermore, given the crucial role of eGFR as a pivotal biomarker in the early detection and diagnosis of CKD, we utilized eGFR to fit a logistic regression model for predicting the 10-year risk of CKD occurrence. This model was used as the baseline for the CKD subgroup prediction task⁸³.

We evaluated the predictive performance of the model by assessing the area under the receiver operating characteristic curve (AUC), sensitivity, and specificity to classify patients with and without disease based on predictive values. The sensitivity and specificity for the FRS, PCE, QRISK3, and SCORE models, were calculated using thresholds of 0.15, 0.075, 0.10, and 0.03, respectively. To evaluate the predictive performance, we obtained the mean and standard deviation (SD) of the five-fold cross-validation. We also plotted receiver operating characteristic curves (ROC) for visual representation. Furthermore, we generated calibration curves and decision curves to evaluate the model. The calibration curve provides insights into the alignment between predicted probabilities and actual outcomes, as measured by the Brier Score (BS). A lower BS indicates a higher degree of consistency, signifying more accurate estimations. On the other hand, the decision curve allows for an evaluation of the model's clinical utility. The larger the area under the decision curve, the greater the practical value of the model in a clinical setting. In this particular model, the training and testing are conducted exclusively based on the fundus images of the left eye. We also trained a model based on fundus images of the right eye to predict the likelihood of major vascular-related events and conducted a Spearman correlation analysis with the results from the left eye.

Association of predicted risks with major vascular-related events

We further verified the association between the predicted score and the incidence of major vascular-related diseases (Fig. 1c). The study population was stratified into low-risk, middle-risk, and high-risk groups based on the predicted risk thresholds of 0.25 and 0.75. We conducted log-rank tests to analyze the incidence of major vascular-related events among these three groups and presented the survival probability using Kaplan–Meier curves. Additionally, the prediction scores were stratified into deciles and the odds ratios (OR) of each decile in comparison with the lowest decile were calculated.

Next, we investigated the disparities in retinal microvascular characteristics among groups with high, middle, and low risks to establish the associations between retinal morphological parameters and the risk of developing major vascular-related events. Kruskal–Wallis test was utilized to compare the retinal microvascular traits among three risk groups, with $p < 0.05$ indicating statistical significance.

Subgroup analysis

In addition to the analysis conducted at the composite event level, subgroup analyses were performed for three selected diseases. Cohorts of stroke, MI, and CKD patients were extracted to analyze the predictive performance of the proposed model on these subgroups. Taking stroke as an example, the sub-cohort was comprised of two groups: individuals with stroke and a control group without any of the three types of diseases.

Each disease subgroup was further categorized into high, middle, and low-risk populations using the same criteria as the main analysis. Additionally, Kaplan–Meier curves were plotted, and statistical tests were performed to examine the differences in retinal features within each of the three cohorts. To investigate the prediction mechanism of the model for three vascular-related diseases based on retinal images, we generated saliency maps. We utilized guided backpropagation, which employs gradients of class probability for each image pixel, to demonstrate how pixels can influence the prediction effects of the model⁸⁴. By visualizing the attention maps of the model for three vascular-related diseases, we aimed to compare the similarities and differences in the model's prediction mechanisms for these distinct vascular-related diseases (Fig. 1d). As examples, we randomly selected four patients from each sub-cohort to demonstrate the specific retinal regions that the model focuses on when predicting different vascular-related diseases. To obtain the model's attentional positions on the retina for each vascular-related disease in the entire population, we further aggregated the saliency maps of each patient by taking the maximum value at each pixel. Our intention was to comprehensively display the regions that may be associated with the outcomes. While the saliency map provides only a qualitative analysis of how the model predicts three vascular-related diseases, our study also included a quantitative analysis of their retinal microvascular characteristics. We compared the retinal parameters of the stroke, MI, and CKD subgroups using the Kruskal–Wallis test, aiming to uncover both the commonalities and differences in retinal morphological features among these subgroups. Patients with multiple coexisting diseases were excluded from the analysis.

We also conducted subgroup analyses to evaluate model performance across age and sex strata. Participants were stratified into three age groups (<45 [young adults], 45–60 [middle-aged adults], >60 [older adults] years)⁸⁵ and by sex (male/female). Model performance metrics (AUC, sensitivity, and specificity) were calculated for each subgroup.

Sensitivity analysis

We performed a sensitivity analysis restricted to White British participants to evaluate potential confounding from population stratification. Model performance metrics (AUC, sensitivity, and specificity) were calculated for this subgroup. Discrimination between this sub-cohort and the full cohort was assessed using a two-sided DeLong's test for AUC differences⁸⁶.

Extraction of retinal image-derived traits

A 32-dimensional feature vector for each patient's retinal image was extracted from the last convolutional layer of the model. We then applied principal component analysis (PCA) to reduce the dimensionality of these features. We extracted principal components that accounted for over 90% of the cumulative variance, which were served as retinal image-derived traits. These traits were then visualized using t-SNE to highlight their potential in distinguishing positive and negative samples⁸⁷. Subsequently, we analyzed the Spearman correlation between these retinal image-derived traits and the retinal morphological parameters and retinal age gap listed in Table 1 to assess the clinical significance of these image-derived features. The p values adjusted for false discovery rate (FDR) correction are reported to indicate the significance of the correlations.

Genetic analysis of retinal image-derived traits

We conducted a genome-wide association study (GWAS) on these retinal-image derived traits (Fig. 1e), employing imputed genotyping data from the UKB study. To account for potential population structure bias, we retained only individuals of White British ancestry and conducted a GWAS analysis

on their retinal image-derived traits based on previous research²⁴. Standard quality control procedures were implemented to exclude samples and SNPs that did not meet specific criteria. Samples with a phenotype deletion rate exceeding 0.05, minor allele frequencies below 0.01, relatedness (PiHat >0.2), and deviations from Hardy-Weinberg equilibrium (HWE $p < 1.0E-06$) were eliminated. For the genetic association analysis, we utilized Plink software (version 1.90 beta, <https://www.cog-genomics.org/plink/>) and assumed an additive genetic model. Covariates such as chronological age, sex, and the top five principal components were incorporated to address population stratification. Considering that the GWAS was performed on five retinal image-derived traits, Bonferroni correction was applied to address the potential for type I errors due to multiple comparisons⁸⁸. Therefore, the standard GWAS significance threshold was set at $1.0E-08$. We utilized LDSC (LD Score) software (version 1.0.1, <https://github.com/bulik/ldsc>) to estimate genomic heritability for GWAS summary statistics of derived traits mentioned above. To functionally characterize the genome-wide significant loci identified in our GWAS analysis, we employed the following approaches: First, we performed functional annotation and gene mapping of image-derived trait-associated SNPs using FUMA (Functional Mapping and Annotation; <https://fuma.ctglab.nl>). Subsequently, we investigated the biological roles of candidate genes through GeneCards (<https://www.genecards.org/>), focusing on their molecular functions and disease relevance. Finally, we examined previously reported phenotype associations for these loci by querying the GWAS Catalog (<https://www.ebi.ac.uk/gwas/>).

To assess the genetic associations between retinal image-derived traits and three vascular-related diseases, we employed two genetic analysis techniques: genetic correlation and colocalization analysis, leveraging publicly available GWAS results primarily sourced from the GWAS Catalog. Specifically, we utilized the LDSC software to quantify genetic correlation. Only high-quality SNPs recorded in the HapMap3 dataset were utilized for estimation, with LD scores derived from the 1KGp3 EUR panel applied for LDSC analysis. The genetic correlation (rg) values and the FDR-adjusted p -values are reported. Moreover, to investigate whether the retinal image-derived traits share common causal variants with three vascular-related diseases, we conducted colocalization analysis using the R package “coloc” (<https://chr1swallace.github.io/coloc/index.html>). This method utilizes Bayesian statistics to estimate the posterior probabilities of five distinct hypotheses regarding the relationship between association signals at a shared locus: PPH0 (No association with either trait), PPH1 (Association with the first trait only), PPH2 (Association with the second trait only), PPH3 (Associations with both traits, but with different causal variants), and PPH4 (Association with both traits due to the same causal variant). Following established conventions, variants with a posterior probability of PPH4 >0.70 were considered as colocalized variants, indicating shared causal variants between the retinal image-derived traits and three vascular-related diseases. Genetic correlation and colocalization analyses were also conducted to explore the genetic associations between retinal imaging-derived traits and retinal morphological characteristics.

Causal effects between retinal image-derived traits and major vascular-related diseases

Two-sample bidirectional Mendelian randomization (MR) analysis was conducted to examine the causal effect between retinal image-derived traits and three vascular-related diseases, including stroke, MI, and CKD (Fig. 1f). In this study, we used the R package “TwoSampleMR” (version 0.5.6) and applied the six default methods: IVW with fixed effects (IVW-FE), IVW with multiplicative random effects (IVW-MRE), MR-Egger, Weighted median, Simple mode, and Weight Mode, with instruments for the diseases obtained from GWAS conducted in non-UKB cohorts (Supplementary Table 25). SNPs that surpassed the significance threshold in each GWAS summary were chosen as instrumental variables (IVs) for the exposure data. These SNPs were subsequently clumped at an $r^2 = 0.1$ within a 1000 kb window size using the LD panel of 1KGp3 to account for linkage disequilibrium and minimize interference. To filter out weak instruments with low statistical power (F -statistic <10), the F -statistic was employed. The

exposure and outcome data were then harmonized based on the same effect alleles, and palindromic SNPs were excluded prior to conducting the MR analysis. To ensure the stability and reliability of the results, a sensitivity analysis was performed on the harmonized data, including heterogeneity and pleiotropy tests⁸⁹. In cases where heterogeneity was detected within a specific set of IVs, precedence was given to the results generated from the IVW-MRE method. Conversely, when pleiotropy was observed, the results obtained from the MR-Egger method were relied upon. If a particular set of IVs passed both tests (i.e., $p > 0.05$), the results from the IVW-FE method were prioritized⁸⁹. To correct for multiple testing across all MR results between five retinal image-derived traits and three vascular-related diseases, we applied the method-level Benjamini-Hochberg False Discovery Rate (BH-FDR) procedure⁹⁰. The statistically significant threshold was set at FDR-corrected $p < 0.05$.

External temporal validation

To assess the generalizability of the proposed model, we conducted external temporal validation using an independent cohort from a subsequent time period, an approach aligned with established validation frameworks in previous studies^{91–94}. The validation data were obtained from participants who underwent retinal imaging during the first repeat assessment visit (2012–2013) of the UK Biobank. To maintain data independence, participants who were part of the initial assessment cohort (2006–2010) were excluded. The cohort selection process for the remaining participants adhered to the same protocol as the primary dataset (Supplementary Fig. 8).

Data availability

The UK Biobank data are available with a proper application process at <https://www.ukbiobank.ac.uk/enable-your-research/apply-for-access>. An interested researcher can contact the corresponding author for additional information.

Code availability

The source codes pertaining to both the proposed model and data analysis in this manuscript are provided at https://github.com/MenglinLu/Retinal_VascularEvents.

Received: 23 December 2024; Accepted: 29 June 2025;

Published online: 14 July 2025

References

- Wong, T. Y. & Mitchell, P. Hypertensive retinopathy. *N. Engl. J. Med.* **351**, 2310–2317 (2004).
- Rim, T. H. et al. Deep-learning-based cardiovascular risk stratification using coronary artery calcium scores predicted from retinal photographs. *Lancet Digital Health* **3**, e306–e316 (2021).
- Tomasoni, M. et al. Genome-wide association studies of retinal vessel tortuosity identify numerous novel loci revealing genes and pathways associated with ocular and cardiometabolic diseases. *Ophthalmol. Sci.* **3**, 100288 (2023).
- Arnould, L. et al. Using artificial intelligence to analyse the retinal vascular network: the future of cardiovascular risk assessment based on oculoscopy? A narrative review. *Ophthalmol. Ther.* **12**, 657–674 (2023).
- Baker, M. L., Hand, P. J., Wang, J. J. & Wong, T. Y. Retinal signs and stroke: revisiting the link between the eye and brain. *Stroke* **39**, 1371–1379 (2008).
- Yusufo, M. et al. Retinal vascular fingerprints predict incident stroke: findings from the UK Biobank cohort study. *Heart* **111**, 306–313 (2025).
- Seidemann, S. B. et al. Retinal vessel calibers in predicting long-term cardiovascular outcomes: the atherosclerosis risk in communities study. *Circulation* **134**, 1328–1338 (2016).
- Liew, G. et al. Fractal analysis of retinal microvasculature and coronary heart disease mortality. *Eur. Heart J.* **32**, 422–429 (2011).

9. Wintergerst, M. W. et al. Retinal vasculature assessed by OCTA in peripheral arterial disease. *Invest. Ophthalmol. Vis. Sci.* **61**, 3203–3203 (2020).
10. Smith, W. et al. Retinal arteriolar narrowing is associated with 5-year incident severe hypertension: the Blue Mountains Eye Study. *Hypertension* **44**, 442–447 (2004).
11. Vaghefi, E. et al. Development and validation of a deep-learning model to predict 10-year atherosclerotic cardiovascular disease risk from retinal images using the UK Biobank and EyePACS 10K datasets. *Cardiovasc. Digital Health J.* **5**, 59–69 (2024).
12. Wagner, S. K. et al. Insights into systemic disease through retinal imaging-based oculomics. *Transl. Vis. Sci. Technol.* **9**, 6–6 (2020).
13. Feuer, D. S. et al. Microvascular dysfunction as a systemic disease: a review of the evidence. *Am. J. Med.* **135**, 1059–1068 (2022).
14. Diaz-Pinto, A. et al. Predicting myocardial infarction through retinal scans and minimal personal information. *Nat. Mach. Intell.* **4**, 55–61 (2022).
15. Wallisch, C. et al. External validation of two Framingham cardiovascular risk equations and the pooled cohort equations: a nationwide registry analysis. *Int. J. Cardiol.* **283**, 165–170 (2019).
16. Qureshi, W. T. et al. Impact of replacing the pooled cohort equation with other cardiovascular disease risk scores on atherosclerotic cardiovascular disease risk assessment (from the Multi-Ethnic Study of Atherosclerosis [MESA]). *Am. J. Cardiol.* **118**, 691–696 (2016).
17. Goff, D. C. et al. 2013 ACC/AHA guideline on the assessment of cardiovascular risk: a report of the American College of Cardiology/American Heart Association Task Force on Practice Guidelines. *J. Am. Coll. Cardiol.* **63**, 2935–2959 (2014).
18. Hippisley-Cox, J., Coupland, C. & Brindle, P. Development and validation of QRISK3 risk prediction algorithms to estimate future risk of cardiovascular disease: prospective cohort study. *BMJ* **357**, j2099 (2017).
19. Guo, S. et al. Association between caliber of retinal vessels and cardiovascular disease: a systematic review and meta-analysis. *Curr. Atheroscler. Rep.* **22**, 1–13 (2020).
20. Cheung, C. Y. A deep-learning system for the assessment of cardiovascular disease risk via the measurement of retinal-vessel calibre. *Nat. Biomed. Eng.* **5**, 498–508 (2021).
21. McGeechan, K. et al. Meta-analysis: retinal vessel caliber and risk for coronary heart disease. *Ann. Intern. Med.* **151**, 404–413 (2009).
22. Cheung, N. et al. Retinal fractals and acute lacunar stroke. *Ann. Neurol.* **68**, 107–111 (2010).
23. Liew, G. et al. Retinal vasculature fractal and stroke mortality. *Stroke* **52**, 1276–1282 (2021).
24. Zekavat, S. M. et al. Deep learning of the retina enables phenome- and genome-wide analyses of the microvasculature. *Circulation* **145**, 134–150 (2022).
25. Cheung, C. Y. et al. Retinal vascular tortuosity, blood pressure, and cardiovascular risk factors. *Ophthalmology* **118**, 812–818 (2011).
26. Allon, R. et al. Retinal microvascular signs as screening and prognostic factors for cardiac disease: a systematic review of current evidence. *Am. J. Med.* **134**, 36–47 (2021).
27. Tseng, R. M. W. et al. Validation of a deep-learning-based retinal biomarker (Reti-CVD) in the prediction of cardiovascular disease: data from UK Biobank. *BMC Med.* **21**, 28 (2023).
28. Joo, Y. S. et al. Non-invasive chronic kidney disease risk stratification tool derived from retina-based deep learning and clinical factors. *npj Digital Med.* **6**, 114 (2023).
29. Sabanayagam, C. et al. A deep learning algorithm to detect chronic kidney disease from retinal photographs in community-based populations. *Lancet Digital Health* **2**, e295–e302 (2020).
30. Zhang, K. et al. Deep-learning models for the detection and incidence prediction of chronic kidney disease and type 2 diabetes from retinal fundus images. *Nat. Biomed. Eng.* **5**, 533–545 (2021).
31. Babenko, B. et al. A deep learning model for novel systemic biomarkers in photographs of the external eye: a retrospective study. *Lancet Digital Health* [https://doi.org/10.1016/S2589-7500\(23\)00022-5](https://doi.org/10.1016/S2589-7500(23)00022-5) (2023).
32. Zhou, Y. et al. A foundation model for generalizable disease detection from retinal images. *Nature* **622**, 156–163 (2023).
33. Ene-Iordache, B. et al. Chronic kidney disease and cardiovascular risk in six regions of the world (ISN-KDDC): a cross-sectional study. *Lancet Glob. Health* **4**, e307–e319 (2016).
34. Gansevoort, R. T. et al. Chronic kidney disease and cardiovascular risk: epidemiology, mechanisms, and prevention. *Lancet* **382**, 339–352 (2013).
35. Vos, T. et al. Global burden of 369 diseases and injuries in 204 countries and territories, 1990–2019: a systematic analysis for the Global Burden of Disease Study 2019. *Lancet* **396**, 1204–1222 (2020).
36. Krittanawong, C., Zhang, H., Wang, Z., Aydar, M. & Kitai, T. Artificial intelligence in precision cardiovascular medicine. *J. Am. Coll. Cardiol.* **69**, 2657–2664 (2017).
37. Berry, C. et al. Small-vessel disease in the heart and brain: current knowledge, unmet therapeutic need, and future directions. *J. Am. Heart Assoc.* **8**, e011104 (2019).
38. Lee, Y. C. et al. Multimodal deep learning of fundus abnormalities and traditional risk factors for cardiovascular risk prediction. *npj Digital Med.* **6**, 14 (2023).
39. Poplin, R. et al. Prediction of cardiovascular risk factors from retinal fundus photographs via deep learning. *Nat. Biomed. Eng.* **2**, 158–164 (2018).
40. Germanese, C. et al. Artificial intelligence-based prediction of neurocardiovascular risk score from retinal swept-source optical coherence tomography–angiography. *Sci. Rep.* **14**, 27089 (2024).
41. Germanese, C. et al. A retinal Oct-Angiography and Cardiovascular STatus (RASTA) dataset of swept-source microvascular imaging for cardiovascular risk assessment. *Data* **8**, 147 (2023).
42. Arnould, L. et al. Prediction of cardiovascular parameters with supervised machine learning from Singapore “I” vessel assessment and OCT-angiography: a pilot study. *Transl. Vis. Sci. Technol.* **10**, 20–20 (2021).
43. Nowroozpoor, A., Gutterman, D. & Safdar, B. Is microvascular dysfunction a systemic disorder with common biomarkers found in the heart, brain, and kidneys?—A scoping review. *Microvasc. Res.* **134**, 104123 (2021).
44. Wang, J. et al. Retinal vascular calibre and the risk of coronary heart disease-related death. *Heart* **92**, 1583–1587 (2006).
45. Liew, G. et al. Retinal microvascular changes in microvascular angina: findings from the Australian Heart Eye Study. *Microcirculation* **26**, e12536 (2019).
46. Wong, T. et al. Retinal arteriolar narrowing and risk of coronary heart disease in men and women—the atherosclerosis risk in communities study. *J. Am. Med. Assoc.* **287**, 1153–1159 (2002).
47. Popovic, N., Radunovic, M., Badnjar, J. & Popovic, T. Fractal dimension and lacunarity analysis of retinal microvascular morphology in hypertension and diabetes. *Microvasc. Res.* **118**, 36–43 (2018).
48. Arnould, L. et al. Retinal vascular network: changes with aging and systemic vascular disease (cardiac and cerebral). *J. Fr. Ophthalmol.* **45**, 104–118 (2021).
49. Mordi, I. R. et al. Prediction of major adverse cardiovascular events from retinal, clinical, and genomic data in individuals with type 2 diabetes: a population cohort study. *Diabetes Care* **45**, 710–716 (2022).
50. Zhu, Z. et al. Retinal age gap as a predictive biomarker of stroke risk. *BMC Med.* **20**, 466 (2022).
51. Zhu, Z. et al. Association of retinal age gap with arterial stiffness and incident cardiovascular disease. *Stroke* **53**, 3320–3328 (2022).

52. Zhang, S. et al. Association of retinal age gap and risk of kidney failure: a UK Biobank study. *Am. J. Kidney Dis.* **81**, 537–544 (2023).
53. Cheung, C. & Wong, T. Is age-related macular degeneration a manifestation of systemic disease? New prospects for early intervention and treatment. *J. Intern. Med.* **276**, 140–153 (2014).
54. Rastogi, N. & Smith, R. T. Association of age-related macular degeneration and reticular macular disease with cardiovascular disease. *Surv. Ophthalmol.* **61**, 422–433 (2016).
55. Tan, Y., Ma, Y., Rao, S. & Sun, X. Performance of deep learning for detection of chronic kidney disease from retinal fundus photographs: a systematic review and meta-analysis. *Eur. J. Ophthalmol.* **34**, 502–509 (2024).
56. Sergouniotis, P. I., Diakite, A., Gaurav, K., Birney, E. & Fitzgerald, T. Autoencoder-based phenotyping of ophthalmic images highlights genetic loci influencing retinal morphology and provides informative biomarkers. *Bioinformatics* **41**, btac732 (2025).
57. Zhu, Z. et al. Shared genetic and experimental links between obesity-related traits and asthma subtypes in UK Biobank. *J. Allergy Clin. Immunol.* **145**, 537–549 (2020).
58. Huang, J. et al. Genomics and phenomics of body mass index reveals a complex disease network. *Nat. Commun.* **13**, 7973 (2022).
59. Kichaev, G. et al. Leveraging polygenic functional enrichment to improve GWAS power. *Am. J. Hum. Genet.* **104**, 65–75 (2019).
60. Liu, M. et al. Association studies of up to 1.2 million individuals yield new insights into the genetic etiology of tobacco and alcohol use. *Nat. Genet.* **51**, 237–244 (2019).
61. Saunders, G. R. et al. Genetic diversity fuels gene discovery for tobacco and alcohol use. *Nature* **612**, 720–724 (2022).
62. Stanzick, K. J. et al. Discovery and prioritization of variants and genes for kidney function in > 1.2 million individuals. *Nat. Commun.* **12**, 4350 (2021).
63. Wuttke, M. et al. A catalog of genetic loci associated with kidney function from analyses of a million individuals. *Nat. Genet.* **51**, 957–972 (2019).
64. Liu, H. et al. Epigenomic and transcriptomic analyses define core cell types, genes and targetable mechanisms for kidney disease. *Nat. Genet.* **54**, 950–962 (2022).
65. Graham, S. E. et al. The power of genetic diversity in genome-wide association studies of lipids. *Nature* **600**, 675–679 (2021).
66. Richardson, T. G. et al. Evaluating the relationship between circulating lipoprotein lipids and apolipoproteins with risk of coronary heart disease: a multivariable Mendelian randomisation analysis. *PLoS Med.* **17**, e1003062 (2020).
67. Sakaue, S. et al. A cross-population atlas of genetic associations for 220 human phenotypes. *Nat. Genet.* **53**, 1415–1424 (2021).
68. Kalantar-Zadeh, K., Jafar, T. H., Nitsch, D., Neuen, B. L. & Perkovic, V. Chronic kidney disease. *Lancet* **398**, 786–802 (2021).
69. Levey, A. S. & Coresh, J. Chronic kidney disease. *Lancet* **379**, 165–180 (2012).
70. Chade, A. R. Small vessels, big role: renal microcirculation and progression of renal injury. *Hypertension* **69**, 551–563 (2017).
71. Feske, S. K. Ischemic stroke. *Am. J. Med.* **134**, 1457–1464 (2021).
72. Coresh, J., Astor, B. & Sarnak, M. J. Evidence for increased cardiovascular disease risk in patients with chronic kidney disease. *Curr. Opin. Nephrol. Hypertens.* **13**, 73–81 (2004).
73. Ko, F. et al. Association of retinal nerve fiber layer thinning with current and future cognitive decline: a study using optical coherence tomography. *JAMA Neurol.* **75**, 1198 (2018).
74. Chua, S. Y. L. et al. Cohort profile: design and methods in the eye and vision consortium of UK Biobank. *BMJ Open* **9**, e025077 (2019).
75. Fu, H. et al. Evaluation of Retinal Image Quality Assessment Networks in Different Color-Spaces. In *Medical Image Computing and Computer Assisted Intervention – MICCAI 2019* (eds Shen, D. et al.) 48–56 (Springer International Publishing, Cham, 2019).
76. Dugas, E., Jorge, J., & Cukierski, W. Diabetic Retinopathy Detection. <https://kaggle.com/competitions/diabetic-retinopathy-detection> (2015).
77. Zhou, Y. et al. AutoMorph: automated retinal vascular morphology quantification via a deep learning pipeline. *Trans. Vis. Sci. Tech.* **11**, 12 (2022).
78. He, K., Zhang, X., Ren, S., & Sun, J. Deep Residual Learning for Image Recognition. In *2016 IEEE Conference on Computer Vision and Pattern Recognition (CVPR)* 770–778 (2016).
79. Huang, G., Liu, Z., Maaten, L.V.D. & Weinberger, K. Q. Weinberger. Densely Connected Convolutional Networks. In *2017 IEEE Conference on Computer Vision and Pattern Recognition (CVPR)* 2261–2269 (2017).
80. Johnson, J. M. & Khoshgoftaar, T. M. Survey on deep learning with class imbalance. *J. Big Data* **6**, 1–54 (2019).
81. Lee, C. et al. Framingham risk score and risk of incident chronic kidney disease: a community-based prospective cohort study. *Kidney Res. Clin. Pract.* **38**, 49–59 (2019).
82. Li, Y. et al. Endothelial function, arterial stiffness and Framingham risk score in chronic kidney disease: a prospective observational cohort study. *Hypertens. Res.* **46**, 868–878 (2023).
83. Levey, A. S. et al. A new equation to estimate glomerular filtration rate. *Ann. Intern. Med.* **150**, 604–612 (2009).
84. Springenberg, J. T., Dosovitskiy, A., Brox, T. & Riedmiller, M. A. Striving for Simplicity: The All Convolutional Net. In *3rd International Conference on Learning Representations, (ICLR) Workshop Track Proceedings* (San Diego, CA, USA, 2015).
85. World Health Organization. *World Report on Ageing and Health 2015* (World Health Organization, 2015).
86. DeLong, E. R., DeLong, D. M. & Clarke-Pearson, D. L. Comparing the areas under two or more correlated receiver operating characteristic curves: a nonparametric approach. *Biometrics* **44**, 837–845 (1988).
87. Van der Maaten, L. & Hinton, G. Visualizing data using t-SNE. *J. Mach. Learn. Res.* **9**, 2579–2605 (2008).
88. Flynn, B. I. et al. Deep learning based phenotyping of medical images improves power for gene discovery of complex disease. *npj Digital Med.* **6**, 155 (2023).
89. Sproviero, W. et al. High blood pressure and risk of dementia: a two-sample Mendelian randomization study in the UK Biobank. *Biol. Psychiatry* **89**, 817–824 (2021).
90. Leonardsen, E. H. et al. Genetic architecture of brain age and its causal relations with brain and mental disorders. *Mol. Psychiatry* **28**, 1–10 (2023).
91. Steyerberg, E. W. & Harrell, F. E. Jr Prediction models need appropriate internal, internal-external, and external validation. *J. Clin. Epidemiol.* **69**, 245 (2015).
92. Ishoi, L. et al. Stratified care in hip arthroscopy: can we predict successful and unsuccessful outcomes? Development and external temporal validation of multivariable prediction models. *Br. J. Sports Med.* **57**, 1025–1034 (2023).
93. de Hond, A. A. et al. Predicting readmission or death after discharge from the ICU: external validation and retraining of a machine learning model. *Crit. Care Med.* **51**, 291–300 (2023).
94. Bonkhoff, A. K. et al. Development and validation of prediction models for severe complications after acute ischemic stroke: a study based on the stroke registry of northwestern Germany. *J. Am. Heart Assoc.* **11**, e023175 (2022).

Acknowledgements

This work was partially supported by the National Key Research and Development Program of China under grant no. 2022YFF1202400 and National Nature Science Foundation of China under grant no. 82272129. We would like to acknowledge the invaluable support of Professor Ching-Yu

Cheng, Cancan Xue, and Quek Ten Cheer from the Singapore National Eye Centre for their assistance with the experiments conducted in this study.

Author contributions

M.L. contributed to the design, drafted the paper, was responsible for the computer programming and the main statistical outcome analyses. Y.M. and H.Z. conceived the study, contributed to the design, data analyses and drafted the paper. Y.Y. provided strategic guidance and oversight. Y.X. and F.W. were the chief investigator, conceived the study, contributed to the design and oversaw the statistical analysis. Z.H. was the chief investigator, conceived the study, led the design and drafted the paper. All authors commented upon and approved the final manuscript.

Competing interests

The authors declare no competing interests.

Additional information

Supplementary information The online version contains supplementary material available at

<https://doi.org/10.1038/s41746-025-01850-5>.

Correspondence and requests for materials should be addressed to Fei Wu or Zhengxing Huang.

Reprints and permissions information is available at <http://www.nature.com/reprints>

Publisher's note Springer Nature remains neutral with regard to jurisdictional claims in published maps and institutional affiliations.

Open Access This article is licensed under a Creative Commons Attribution-NonCommercial-NoDerivatives 4.0 International License, which permits any non-commercial use, sharing, distribution and reproduction in any medium or format, as long as you give appropriate credit to the original author(s) and the source, provide a link to the Creative Commons licence, and indicate if you modified the licensed material. You do not have permission under this licence to share adapted material derived from this article or parts of it. The images or other third party material in this article are included in the article's Creative Commons licence, unless indicated otherwise in a credit line to the material. If material is not included in the article's Creative Commons licence and your intended use is not permitted by statutory regulation or exceeds the permitted use, you will need to obtain permission directly from the copyright holder. To view a copy of this licence, visit <http://creativecommons.org/licenses/by-nc-nd/4.0/>.

© The Author(s) 2025